Available online at www.sciencedirect.com
SCIENCE DIRECT
Fuel 84 (2005) 2026–2038
FUEL
www.fuelfirst.com

Fuel size effect on pinewood combustion in a packed bed

Yao Bin Yang*, Changkook Ryu, Adela Khor, Vida N. Sharifi, Jim Swithenbank

Department of Chemical and Process Engineering, Sheffield University Waste Incineration Centre (SUWIC), Sheffield University, Mappin Street, Sheffield S1 3JD, UK

Received 15 September 2004; received in revised form 22 April 2005; accepted 26 April 2005
Available online 6 June 2005

Abstract

In this paper, particle size effect on pinewood combustion in a stationary packed bed was investigated. Mass loss rate, temperature profile at different bed locations and gas compositions in the out-of-bed flue gases were measured at a fixed primary air flow rate. Pinewood cubes was fired with size ranging from 5 to 35 mm. A unique numerical model applicable to thermally thick particles was proposed and relevant equations were solved to simulate the non-homogeneous characteristics of the burning process. It is found that at the operating conditions of the current study, smaller particles are quicker to ignite than larger particles and have distinctive combustion stages; burning rate is also higher with smaller fuel size; and smaller fuels have a thinner reaction zone and result in both higher CO and CH_4 concentrations in the out-of-bed flue gases; on the other hand, larger particles produced a higher flame temperature and result in higher H_2 concentration in the flue gases. Larger particles also cause the combustion process becoming more transient where the burning rate varies for most part of the combustion process.
© 2005 Elsevier Ltd. All rights reserved.

Keywords: Combustion; Fuel size; Pinewood; Mathematical modelling

1. Introduction

Biomass is playing an important role for domestic heating and power generation, especially in some European countries. With the increasing concerns over global warming from fossil fuel combustion in recent years, some organisations have proposed energy crops to cut down the net CO_2 emission to the atmosphere [1,2]. In a broad sense, biomass fuels range from pruning waste, industrial and agrarian residuals, waste wood, cultivated crops to sewage sludge from domestic and industrial water treatment plants and paper industry. Although biomass burning is as old as humankind's history, the modern large-scale production of heat and electricity from biomass need sophisticated technology to control the process to minimise its environmental effects and promote efficiency. In most cases, raw biomass fuels cannot be burned as they are. Instead they need some pre-treatment. Pelletisation is now an accepted practice before biomass fuels are burned in furnaces or on beds. One of the key questions arises from this is what are the effects of the particle size on the combustion behaviour and how to assess the optimum pellet size from economic and technical points of view.

In this paper the size effect of pinewood cubes is investigated both theoretically and experimentally for packed bed combustion. Pinewood fuel is easy to prepare and can be cut into different sizes and shapes and is a good simulation of pelletised biomass fuels. The latter are normally difficult and expensive to prepare in terms of size variation. General combustion behaviours of biomass fuels on packed beds have been studied by a number of researchers. Gort [3] had conducted a series of tests on combustion of wood chips under different operating conditions. Friberg and Blasiak [4] measured the mass flux and stoichiometry of conversion gas from three different wood fuels as function of volume flux of primary air. Rönnbäck et al. [5] studied the influence of primary airflow and particle properties on the ignition front, its temperature and on the composition of the exiting gases in a biomass fuel bed. Saastamoinen et al. [6] investigated the propagation of ignition front in beds of wood particles where the effect of air flow, moisture, particle size, density and wood species were considered. Van der lans et al. [7]

* Corresponding author. Tel.: +44 114 2227500; fax: +44 114 2227501.
E-mail address: y.b.yang@sheffield.ac.uk (Y.B. Yang).

0016-2361/$ - see front matter © 2005 Elsevier Ltd. All rights reserved.
doi:10.1016/j.fuel.2005.04.022

Nomenclature

C constant; molar fractions of species (fuel, oxygen)
C_{fuel} fuel concentration, kg/m^3
C_{pg} specific heat capacity of the gas mixture, J/(kg K)
C_{mix} mixing-rate constant
D_{ax} in-flow dispersion coefficient in bed, m^2/s
D_g molecular diffusion coefficient of volatile hydrocarbons in air, m^2/s
D_{ig} dispersion coefficients of the species $\boldsymbol{Y_{ig}}$, m^2/s
d_p particle diameter, m
d_{pore} pore diameter in particle, m
D_r cross-flow dispersion coefficient in bed, m^2/s
I radiation heat flux, W/m^2
$\boldsymbol{H_g}$ gas enthalpy, J/kg
$\boldsymbol{H_s}$ solid-phase enthalpy, J/kg
h_s' convective heat transfer coefficient between solid and gas, W/m^{2}K
k_a absorption coefficient of radiation, 1/m
k_d rate constants of char burning due to diffusion, kg/atm m^2 s
k_r rate constants of char burning due to chemical kinetics, kg/atm m^2 s
k_s scattering coefficient of radiation, 1/m
k_v rate constant of devolatilisation, s^{-1}
M moisture fraction in solid
M_0 initial moisture fraction in solid
p_g gas pressure, Pa
Q_h heat loss/gain of the gases, W/m^3
Q_{sh} thermal source term for solid phase, W/m^3
q_r radiative heat flux, W/m^2
R_{mix} mixing-rate of gaseous phase in the bed, kg/m^3 s
S stoichiometric coefficients in reactions
S_a particle surface area, m^2
S_{sg} conversion rate from solid to gases due to evaporation, devolatilisation and char burning, kg/m^3 s
Sy_{ig} mass sources due to evaporation, devolatilisation and combustion, kg/m^3 s
Sy_{is} source term, kg/m^3 s
t time instant, s
T_g gas temperature, K
T_s solid temperature, K
T_{s0} solid temperature at the particle surface, K
$\mathbf{V_B}$ velocity of a moving boundary, m/s
$\mathbf{V_g}$ superficial gas velocity (vector), m/s
VM volatile matter in solid
VM_0 initial volatile matter in solid
$\boldsymbol{Y_{ig}}$ mass fractions of gaseous compositions (CO, CO_2, O_2, CH_4, H_2, etc.)
$\boldsymbol{Y_{is}}$ mass fractions of particle compositions (moisture, volatile, fixed carbon and ash)
y^+ distance above the bed-top surface, m;
ε_p solid emissivity
σ_b Boltzmann radiation constant, 5.86×10^{-8} W/m^{2}K^4
void fraction in the bed
ρ_g gas density, kg/m^3
ρ_s solid material density in the bed, kg/m^3
λ_{ax} in-flow diffusion coefficient in bed, W/m K
λ_c thermal conductivity of char, W/m K
λ_g thermal dispersion coefficient, W/m K
λ_r cross-flow diffusion coefficient in bed, W/m K
λ_s solid-phase thermal conductivity in bed, W/m K
λ_{wood} effective thermal conductivity of the wood material, W/m K

performed experiments on straw combustion in a 15 cm diameter and 137 cm long vertical reactor where both air flow rate and inlet air temperature were varied. Channelling phenomena in packed beds have been studied by Yang et al. [8,9]. Other important works were summarised by Thunman [10], Thunman et al. [11] and Peters [12].

Though those studies provide important information on biomass combustion in packed beds, the obtained data were still very limited and in most cases only ignition speed and maximum flame-front temperature were reported. Results concerning particle size effect were also inconsistent. For example, Gort [3] and Rönnbäck [5] have reported increased ignition speed for larger particles in the size range of 10–30 mm while Peters [12] reported the maximum ignition rate was obtained at 15 mm in the size range of 5–25 mm. On the other hand, Friberg et al. [4] demonstrated decreasing burning rate as particles size increased.

Current work focuses on both experimental and theoretical studies for packed bed combustion and particle sizes from 5–35 mm were used. For the experimental work, a pot reactor of 0.2 m in diameter and 1.5 m in height was used. Some researchers [13] have used Thermogravimetric System (TGS) to study biomass combustion which gives a strictly controlled environment. The benefit of employing a pot reactor, however, is that it provides more realistic results for practical furnaces.

For mathematical modelling, a unique numerical model was proposed and detailed equations governing the fluid flow, heat and mass transfer between solid and gaseous phases were employed and solved. The advantage of theoretical study lies in its ability to reveal the detailed structure of the burning process inside a solid bed, such as reaction zone thickness, combustion staging, gas emission and char burning characteristics, thus contributing to better understanding and controlling of the process. These

Table 1
Proximate and ultimate analysis of willow wood fuel

Moisture (wt%)	Volatile (wt%)	Fixed carbon (wt%)	Ash (wt%)	C (wt%)	H (wt%)	O (wt%)	LCV (MJ/kg)
7.5	79.7	12.7	0.1	47.9	6.2	38.3	17.6

parameters are otherwise hard to obtain by conventional experimental techniques.

2. Experimental facilities

A fixed-bed reactor was employed to burn the pinewood fuel. This reactor has been used in previous studies [14–16]. It was a vertical cylindrical combustion chamber suspended from a weighing scale. The height of the chamber was 1.5 m with an inner diameter of 200 mm. It consisted of an interior tube surrounded by a thick layer of insulating material and an external casing. The grate was located at the bottom of the chamber and consisted of a perforated plate made from stainless steel, with approximately 700 holes of 2 mm diameter, representing 7% open area. Thermocouples were used to monitor the temperature of primary airflow, temperature inside the bed at different height levels and temperature of the flue gases. There was a gas-sampling probe inside the chamber at 430 mm above the grate. The main components of the gas measurements of interest were O_2, CO, CO_2.

A gas burner was placed at a 45° angle toward the waste at 750 mm above the grate. The gas burner was used to initiate the burning process of the fuel sample and switched off after a steady combustion was observed. Primary air was fed from the bottom of the fixed bed reactor through the grate without pre-heating.

The pinewood fuel was cut into four different sizes: 5×5×5, 10×10×10, 20×20×20 and 35×35×35 mm. Proximate and ultimate analysis of the fuel are shown in Table 1. Density of the fuel material was measured being 820 kg/m^3 and the bulk density in packed state is around 290 kg/m^3, giving a bed porosity of 0.65. For each run 3.8 kg of fuel was used and the initial bed height was around 410 mm. The primary air employed was 0.1 kg/m^2 s at room temperature for all the cases.

Fig. 1 illustrates the packed bed dimensions and operating conditions.

3. Mathematical model for biomass combustion in a packed bed

Peters [12] summarized the previous mathematical models on packed bed combustion. Those models can be generally classified into four categories: continuous-medium models [17–19] where the solid bed was treated as a continuous medium; neighbouring-layers models [20,21] where the packed bed above the grate was divided into four layers representing fuel, drying, pyrolysis and ash; well-stirred reactor models [22,23] where the bed was simulated by a cascade of well-stirred reactors; and the 1d+1d model [24] where a one-dimensional and transient single-particle model in spherical coordinates was implemented in a transient one-dimensional fuel-bed model.

The model used in current work is based on the governing equations proposed by Peters [25] for both the gas and solid phases in a moving bed and the previous modelling works of the authors [8–16]. The major difference of the current model from all the previous models is that it calculates both outside and inside the particles and thus fully accounts for the inhomogeneous nature of the bed and the effect of thermally thick particles. Compared to the 1d+1d model [24] the proposed mathematical method provides a more realistic simulation to the real combustion bed.

Illustration of the model concept is shown in Fig. 2. A packed bed consists of particles and the voids between them (Fig. 2a). By discretising the bed, three types of cells emerge: void cells, boundary cells and inner cells (Fig. 2b). The void cells are where the gas-flow passes and the inner cells are inside-particle cells. Boundary cells are solid-phase cells neighbouring the gas-flow around the particle outer surfaces. Thus, a particle is represented by a set of inner and boundary cells and the bed an assembly of inner, boundary and void cells.

For each cell, the law of conservation in momentum, energy and chemical species is applied and different schemes are employed, depending on the cell type. For example, for an inner cell heat conduction is the only heat transfer mode. But for a boundary cell, heat conduction, convection and radiation all play a part in the heat transfer

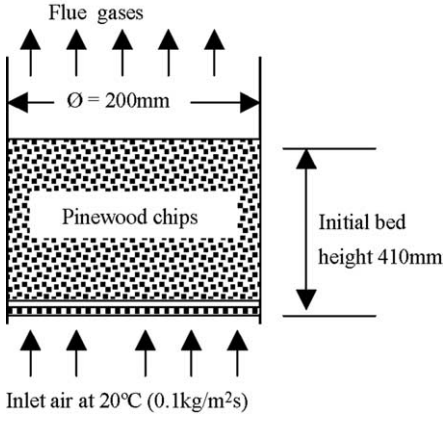

Fig. 1. The employed packed bed dimensions and operating conditions.

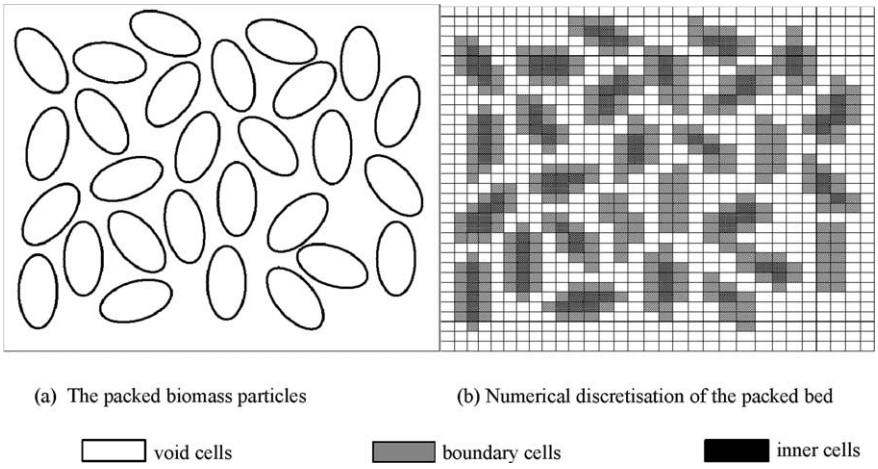

Fig. 2. Illustration of the model concept for thermally-thick particles.

process. For the void cells, apart from all these three heat transfer modes, turbulence effect is also included.

3.1. Transport equations for the gas phase in the void cells

The equations include mass continuity, momentum conservation, heat transfer and species transport.

$$\text{Continuity}: \quad \frac{\partial(\phi\rho_g)}{\partial t} + \nabla(\phi\rho_g(\mathbf{V_g} - \mathbf{V_B})) = S_{sg} \tag{1}$$

where $\mathbf{V_g}$ is the gas velocity and $\mathbf{V_B}$ the velocity of a moving boundary. The source term S_{sg} is the conversion rate from solid to gas due to moisture evaporation, devolatilisation and char combustion.

$$\text{Momentum}: \quad \frac{\partial(\phi\rho_g\mathbf{V}_g)}{\partial t} + \nabla(\phi\rho_g(\mathbf{V}_g - \mathbf{V}_B)\mathbf{V}_g) = -\nabla p_g + F(\mathbf{v}) \tag{2}$$

where $F(\mathbf{v})$ represents resistance of solids to fluid flow in a porous medium and is calculated by Ergon's equations [26,27].

$$\text{Species transport}: \frac{\partial(\phi\rho_g\mathbf{Y}_{ig})}{\partial t} + \nabla(\phi\rho_g(\mathbf{V}_g - \mathbf{V}_B)\mathbf{Y}_{ig}) = \nabla(D_{ig}\nabla(\rho_g\mathbf{Y}_{ig})) + S_{yig} \tag{3}$$

where $\boldsymbol{Y_{ig}}$ is mass fractions of individual species (e.g. H_2, H_2O, CO, CO2, C_mH_n, …). The source term S_{yig}accounts for mass sources of the individual species during evaporation, devolatilization and the combustion of volatile gases and char.

The fluid dispersion coefficient D_{ig} consists of diffusion and turbulent contributions. For $\mathrm{Re} > 5$, the corresponding cross-flow and in-flow dispersion coefficients are given by the following Eqs. [28]:

$$D_r = E^0 + 0.1 d_p|\mathbf{V}_g| \tag{4a}$$

$$D_{ax} = E^0 + 0.5 d_p|\mathbf{V_g}| \tag{4b}$$

where E^0 is the effective diffusion coefficient.

$$\text{Energy}: \quad \frac{\partial(\phi\rho_g H_g)}{\partial t} + \nabla\cdot(\phi\rho_g(\mathbf{V_g} - \mathbf{V_B})H_g) = \nabla\cdot(\lambda_g\nabla T_g) + S_a h_s'(T_{so} - T_g) + Q_h \tag{5}$$

where H_g represents gas enthalpy, λ_g the thermal dispersion coefficient and Q_h, the heat gain of the gas phase due to heat release during combustion. The thermal dispersion coefficient λ_g consists of diffusion and turbulent contributions in a similar way as species dispersion, and can be expressed as [28]:

$$\lambda_r = \lambda_g^0 + 0.1 d_p|\mathbf{V_g}|\rho_g C_{pg} \tag{6a}$$

$$\lambda_{ax} = \lambda_g^0 + 0.5 d_p|\mathbf{V_g}|\rho_g C_{pg} \tag{6b}$$

Where λ_g^0 is the effective thermal diffusion coefficient.

3.2. Governing equations for solid phase cells

Volume shrinkage of biomass particles during combustion is calculated by the following equation:

$$\frac{V}{V_0} = 1 - a_1(M_0 - M) - a_2(VM_0 - VM) - a_3(C_0 - C) \tag{7}$$

where V and V_0 represent the current and initial volumes of a particle and a_1, a_2, a_3 are shrinkage factors during moisture evaporation, volatile release and char burnout respectively. Their values are chosen such that $a_1 = 1$ represents the volume of the particle shrinking linearly with moisture loss and $a_1 = 0$ means no volume shrinkage occurring during evaporation. The same principle applies to a_2 and a_3.

Energy conservation for the boundary cells is described by

$$\frac{\partial(\rho_s H_s)}{\partial t} = \nabla(\lambda_s\nabla T_s) - S_a h_s'(T_{so} - T_g) + \nabla q_r + Q_{sh} \tag{8}$$

where H_s presents the solid-phase enthalpy, λ_s is the effective thermal conductivity of the solid bed and q_r the radiative heat flux. The source term Q_{sh} summarises heat effects due to moisture evaporation and heterogeneous combustion.

For inner cells the above equation is reduced to

$$\frac{\partial(\rho_s H_s)}{\partial t} = \nabla(\lambda_s \nabla T_s) + Q_{sh} \tag{8a}$$

by dropping out the radiation and convection terms.

The effective thermal conductivity of the solid material consists of a conductive and a radiative contribution [29]:

$$\lambda_s = \varepsilon_p \lambda_g^0 + \eta\lambda_{\text{wood}} + (1-\eta)\lambda_C + \lambda_{\text{rad}} \tag{9}$$

where ε_p is the local porosity of the solid cell and λ_{wood}, λ_{C} are thermal conductivity of the wood and char. The radiative part is calculated as following [30],

$$\lambda_{\text{rad}} = 4 \times \varepsilon_{\text{rad}} \sigma_b T_s^3 \text{d}_{\text{pore}} \tag{10}$$

where ε_{rad} is the emissivity of the pores inside a particle and d_{pore} the diameter of the pores.

The solid fuel is assumed to consist of four components: moisture, volatile matter, fixed carbon and ash. The incineration process of solid wastes can be divided into four successive sub-processes: evaporation of moisture from the solids, volatile release/char formation, burning of the hydrocarbon volatiles in the gaseous space, and the combustion of char particles. Calculation of the rates for moisture evaporation, devolatilisation and char burning can be found in the works of Yang et al. [14,15].

3.3. Mixing of volatile gases with under-grate air

Gaseous fuels released from the devolatilization process have first to mix with the surrounding air before any combustion of them can take place. Obviously the burning of the volatile hydrocarbon gases is limited not only by the reaction kinetics (temperature dependent) but also by the mixing-rate of the gaseous fuel with the under-grate air flow. The mixing rate inside the bed is assumed to be proportional to energy loss (pressure drop) through the bed and can be expressed as [31]:

$$R_{\text{mix}} = C_{\text{mix}}\rho_g \left\{ 150\frac{D_g(1-\phi)^{2/3}}{d_p^2\phi} + 175\frac{V_g(1-\phi)^{1/3}}{d_p\phi} \right\} \times \min\left\{ \frac{C_{fuel}}{S_{fuel}}, \frac{C_{O2}}{S_{O2}} \right\} \tag{11}$$

Where C_{mix} is an empirical constant, D_{g} the molecular diffusivity of the combustion air, V_g the air velocity, d_{p} the particle diameter, ϕ the local void fraction of the bed, C the molar fractions of the gaseous reactants and S their stoichiometric coefficients in the reaction.

In the free-board area immediately next to the bed surface, 'flame tongues' shoot out of the bed surface and the mixing rate of the volatile gases with surrounding air decreases with increasing distance from the bed surface. Detailed CFD calculations with simulated particle beds were conducted and have produced the following correlation between mixing rate and the distance from the bed-top [14]:

$$R_{\text{mix}} = R'_{\text{mixo}}(2.8\text{e}^{-0.2y++} - 1.8\text{e}^{-2y++})\min\left\{ \frac{C_{fuel}}{S_{fuel}}, \frac{CO2}{SO2} \right\} \tag{12}$$

and

$$y^{++} = y^{+}/d_p \tag{13}$$

where R'_{mixo} is calculated from Eq. (11) without the species concentration terms at the bed surface. y^+ denotes the physical distance from the bed top.

The actual combustion rate of the volatile gases is taken as the minimum between the mixing rate calculated by the above equations and the kinetic rate. Calculation of the latter can be found in Ref. [15].

3.4. Radiation heat transfer in the bed

Radiation is the major mechanism of heat transfer between solid particles in a packed bed. The widely used flux model [32] is employed:

$$\frac{dI_{xi}^{+}}{dx_i} = -(k_a + k_s)I_{xi}^{+} + \frac{1}{2N}k_a E_b + \frac{1}{2N}k_s \sum_{i=1}^{N}(I_{xi}^{+} + I_{xi}^{-}) \tag{14a}$$

$$-\frac{dI_{xi}^{-}}{dx_i} = -(k_a + k_s)I_{xi}^{-} + \frac{1}{2N}k_a E_b + \frac{1}{2N}k_s \sum_{i=1}^{N}(I_{xi}^{+} + I_{xi}^{-}) \tag{14b}$$

where N is the total number of space discretisation and I_{xi}^{+} and I_{xi}^{-} ($i=1,N$) are the radiation fluxes in the positive and negative directions respectively of each discretisation. E_b represents the black-body radiation. k_a and k_s denote the absorption and scattering coefficients. In this work k_s is assumed to be zero and k_a is approximated by the following equation [19]:

$$k_a = -\frac{1}{d_p}\ln(\phi) \tag{15}$$

3.5. Particle size effects

According to the governing equations described above, particle size affects the combustion in five different ways. First is the two-phase heat and mass transfer (between the gas and solid), as indicated by the second RHS term in Eq. (8). These convective processes occur at the particle external surfaces and the rates are approximately inversely proportional to the particle diameter. Therefore, particles of

a smaller size can enhance the moisture evaporation and char burning rates in the bed. Temperature difference between the solid and gas is also smaller for small particles.

The second effect is on the radiation heat transfer, as indicated in Eq. (15) where the bed absorption coefficient to radiation flux is inversely proportional to particle diameter. This means that a bed of smaller particles absorbs radiation more quickly. But the radiation flux, on the other hand, is less absorbed by a packing of larger particles and hence penetrates a longer distance in the bed. This can produce a thicker flame front in the bed and affects the temperature and gas concentration profiles as a consequence.

The third effect is on the turbulent dispersion of energy and gas species in the packed bed. As indicated in Eqs. (4) and (6), both the effective thermal and fluid dispersion coefficients are proportional to particle diameter. Larger particles produce larger-scale turbulence in the local bed structure and facilitate the cross-flow and inflow mixing in the gas phase. As a result, the reaction zone in the bed can be thicker for larger particles and thinner for smaller particles.

The fourth effect is on the burning rate of volatile gaseous fuel both in the voids of the bed and in the immediate area above the bed. The process is basically diffusion-controlled. As indicated in Eqs. (11)–(13), the mixing rate of the fuel gases with air flow from under the grate is a function of particle size and small particles produce higher rate the other conditions being the same and hence intensity the combustion in the gas phase.

The fifth effect lies in the non-uniform temperature distribution inside a particle. A large particle tends to be thermally thick and large temperature gradient exists inside the particle, especially during the period of ignition or around the flame front. This affects the moisture evaporation rate and devolatilisation rate of the particle, which are strong functions of local solid temperature.

4. Solving technique and boundary conditions

The solving technique is based on the SIMPLE algorithm [33] for the governing equations of both gas and solid phases. The whole bed is discretised into around 300 cells along the bed height and time-dependant numerical solution is sought for a set of parameters, including gas and solid temperatures, concentration of gaseous species (CH_4, CO, H_2, O_2, CO_2, H_2O and N_2), gas velocity and the four components of the solid phase (water, volatile matter, fixed carbon and ash). The calculation also gives detailed process-rate profiles such as hydrocarbon-gas production and consumption, char burning rate, radiation absorption, etc. The radiation equations are solved by the fourth-order Runge-Kutta method [34]. The total number of space discretisation in Eq. (14) is taken as two.

The composition of the volatile gases released during devolatilisation process is assumed to be 36% CH_4, 34% CO, 9.5% H_2, 13% CO_2 and 7.5% H_2O by volume. This is based on both elemental and heat balances so that the total masses of C, H and O in the product molecules equal to the those from the ultimate analysis and the total heat from the burning of the combustible gases equals to the calorific value of the volatiles, which can be deduced from the LCV of the fuel.

Particle shrinkage factors a_1, a_2 and a_3 in Eq. (7) are taken as being 0.8. Other fuel properties employed in the model are: the porosity of the wood particle $\varepsilon_p = 0.6$; wood conductivity $\lambda_{wood} = 0.2$ W/m K; char conductivity $\lambda_C = 0.1$ W/m K; particle pore size $d_{pore} = 50 \times 10^{-6}$ m; and pore cell emissivity $\varepsilon_{rad} = 0.9$. These data are based on reference [12].

The empirical mixing coefficient, C_{mix}, in Eq. (11) is taken as 0.5 [14,15]; The gas-to-solid heat transfer coefficient, h_s' in Eqs. (5) and (8) is calculated from Nu $(= d_p h_s'/\lambda_g) = 2 + 1.1 Pr^{1/3} Re^{0.6}$ [28]. The fuel devolatilisation rate parameters are those of Alves and Figueiredo [15,35] where $k_v = 7.0 \times 10^4 \exp(9977/T_s)$ and the kinetic rate of char combustion, $k_r = 2.3\ T_s \exp(-11100/T_s)$ [15].

The fuel is assumed to be ignited by over-board radiation at a temperature of 1173 K with emissivity of 0.8. This radiation source is present for the whole combustion processes. Primary air at 20 °C enters the bed from under the grate. Initial bed height is taken at 410 mm. The combustion starts at the bed top and the bed height falls as the flame front travels down towards the grate.

Boundary conditions: at the upper boundary, gradients of the gaseous temperature, concentrations and velocity are assumed to be zero (the second-type boundary). For the solid phase, the third-type boundary is assumed at both the bottom of the bed and the top surface for temperature (conduction and radiation heat exchange with the grate and over-bed radiation source are considered).

5. Experimental results

5.1. Mass loss history

Fig. 3 shows the mass loss history of fuel expressed as percentage of remaining mass on the bed as a function of reaction time. After switching on the over-bed gas-burner for initiating the reactions ($t = 0$ min), there was an initial ignition period before a steady stage was reached. For the 5 mm pinewood fuel, the initial mass loss was quick, reaching a steady state at $t = 2$ min. For the 10 mm pine wood cubes, the initial mass loss rate was slightly slower, reaching a steady state at $t = 3.5$ min; For the 20 mm particle size, it was only after $t = 7$ min that the mass loss rate reached a steady state. The 35 mm pinewood produced the longest ignition period (15 min) before a fully steady combustion stage was reached.

After the initial ignition period, a linear decrease in the total mass of the bed fuel was observed. Depending on the particle size, the length of this constant burning period

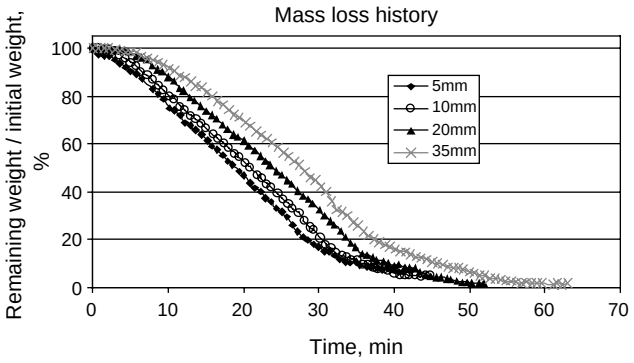

Fig. 3. Mass loss history as a function of reaction time.

ranged from 23 to 15 min, with the largest particles having the shortest period of constant burning.

Further on as the reaction time increased, the rate of the bed mass loss slowed down. For the small pinewood cubes of 5 mm, this final period of combustion was about 13 min before the whole combustion completed. For the 10 mm fuels, it increased to 15 min and for 20 mm, the final burning period further increased to 18 min. The largest fuel size, 35 mm, featured the longest final burning period of 25 min.

It was clear that the total burning time increased with increase in the fuel particle size. The obtained value was 42, 45, 50 and 57 min respectively for the pinewood of 5, 10, 20 and 35 mm.

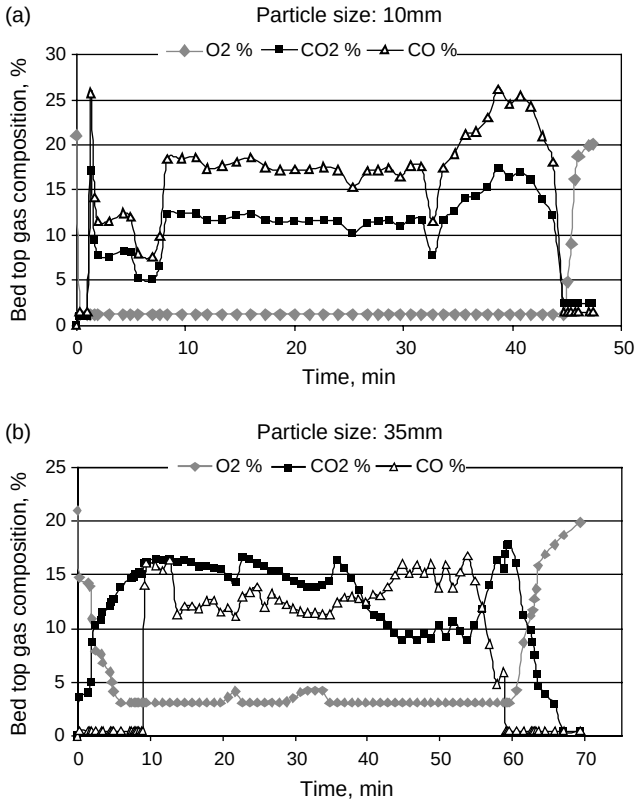

Fig. 4. Gas composition in the flue gases out of the bed top vs. reaction time. (a) Fuel size 10 mm; (b) fuel size 35 mm.

5.2. Gas composition in the out-of-bed flue gases

Fig. 4 shows the gas composition in the flue gases out of the bed top as a function of time for 10 and 35 mm pinewood chips. For the smaller size (Fig. 4a), the O_2 concentration in the flue gases quickly dropped from the ambient level of 21% to a minimum level (~1.0%) as soon as the gas-burner for ignition was switched on. There was an initial sharp spike for both CO and CO_2 concentrations, followed by a relatively steady and short period of low levels of CO and CO_2. Further on at about 8 min, the measured CO and CO_2 rose to an elevated steady state of 18 and 12%, respectively, while the O_2 remained unchanged (1.0%). At about 34 min, both CO and CO_2 began to rise again and peaked at 40 min with a value of 25 and 17%, respectively before quickly reducing to 0% at 44 min to complete the combustion.

For the 35 mm pinewood chips, the gas composition profile against the time (Fig. 4b) was different from the case of 10 mm chips in two ways: firstly the variation with time in the flue gas O_2 and CO_2 concentrations was less intensive during both the initial ignition stage and the final burnout stage; secondly, the levels of O_2 and CO_2 concentrations were higher while the CO concentration was lower during the major stead-state burning period. The CO_2 level was 14% on average compared to 12% and CO 13.5% on average compared to 18% for the 10 mm fuel.

5.3. Temperature profile in the bed

Fig. 5 shows the measured bed temperature against time at different bed heights above the grate for chip sizes of 10

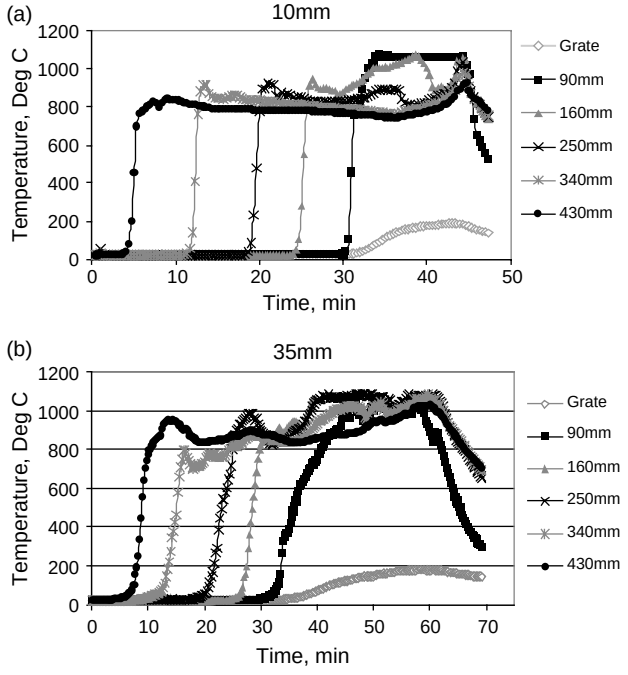

Fig. 5. Bed temperature vs. reaction time at different bed heights above the grate. (a) Fuel size 10 mm; (b) fuel size 35 mm.

and 35 mm. For the smaller pinewood (Fig. 5a), local bed temperature rose sharply from room level to a peak value as high as 910 °C as the flame front passed, then dropped slightly to a lower but stable level around 800 °C. It can be deduced that the flame downward propagation speed was 14.5 mm/min and the average time span for the local temperature rising from the ambient level to the peak level was 2.5 min, giving the flame front thickness of 36 mm (3.6 times the particle size). As the combustion approached the final stage (after $t=30$ min), the bed temperature rose to an even higher level of around 1100 °C, presumably as a result of char burning.

For the largest size of 35 mm (Fig. 5b), two differences can be noticed in the temperature profile from the case of 10 mm size. The first is the longer time span for the rising of local temperature from ambient level to the maximum point as the flame front passes. An average of 6 min was recorded (compared to 2.5 min for the 10 mm particles). The flame downward propagation speed is calculated being 13 mm/min, thus the flame front thickness is deduced to be 78 mm, or 2.2 times the original particle size.

The second difference is the measured maximum temperature level. The 35 mm pinewood produced a higher flame temperature than that for the 10 mm pinewood, reaching 980 °C at the flame front compared to 910 °C with 10 mm (excepting the final char burning stage).

6. Modelling results and comparison with experiments

6.1. Calculated process rates

Fig. 6(a) and (b) demonstrate the moisture evaporation rate distribution inside the bed as a function of time for the 10 and 35 mm fuels. For the 10 mm fuel (Fig. 6a), the upper boundary of the major moisture evaporation zone lies about 50 mm below the bed top and the zone extends 70 mm downward. The maximum local evaporation rate in the

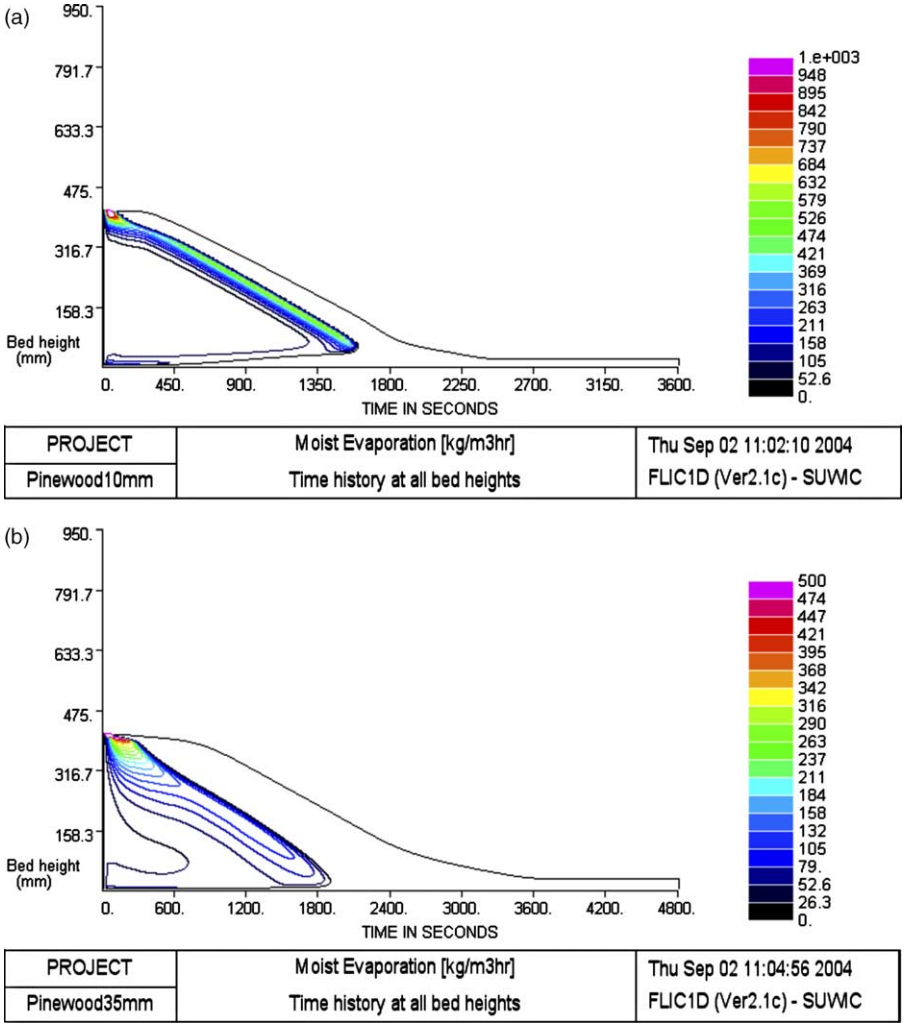

Fig. 6. Calculated process rate profiles in the bed vs. reaction time. (a) Moisture evaporation rate (10 mm); (b) moisture evaporating rate (35 mm); (c) Devolatilisation rate (10 mm); (d) devolatilisation rate (35 mm); (e) char burning rate (10 mm); (f) char burning rate (35 mm).

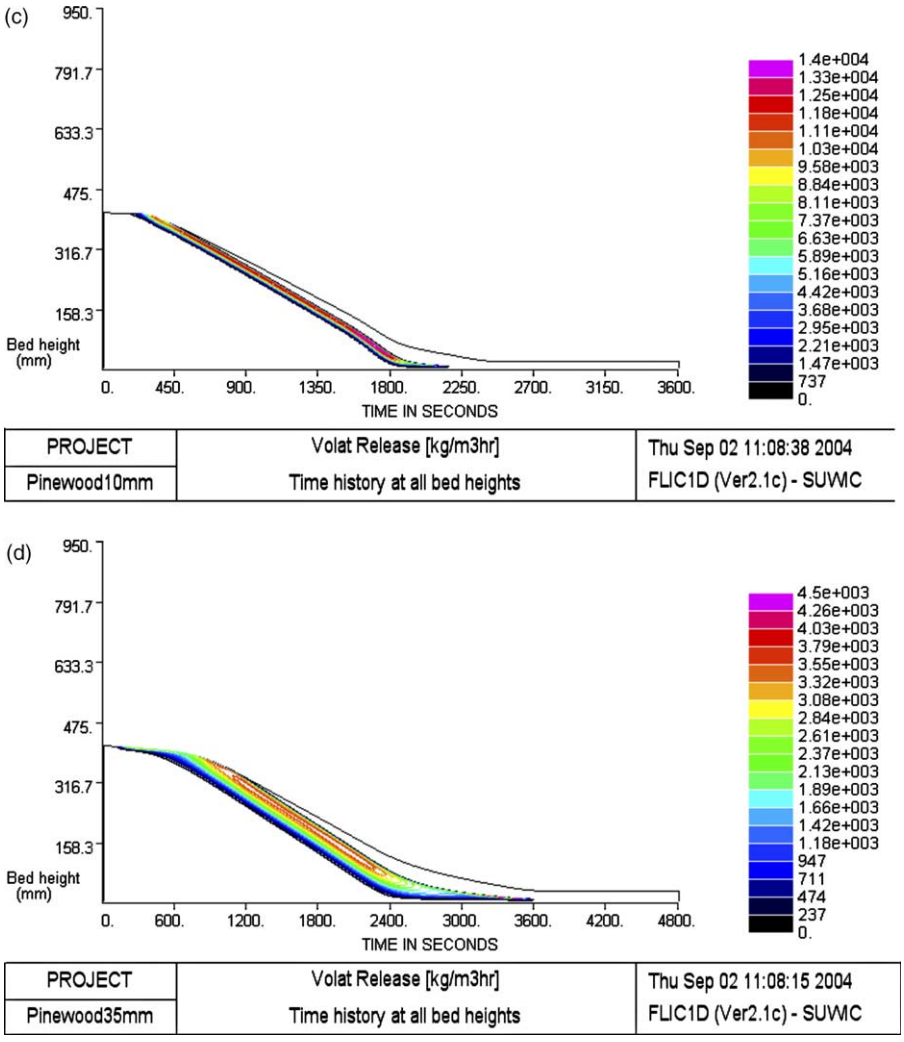

Fig. 6 (*continued*).

constant stage is around 550 kg/m^{3}h; for the 35 mm fuel (Fig. 6b), the upper boundary of the evaporation zone lies around 140 mm below the bed top and the zone extends 125 mm downwards. The maximum local rate in the constant stage is around 100 kg/m^{3}h, only a fifth of that with the 10 mm fuel.

Fig. 6(c) and (d) demonstrate the devolatilisation rate distribution inside the bed as a function of time for the two particle sizes. For the 10 mm fuel, the upper boundary of the major devolatilisation zone moves away from the bed top as the combustion proceeds and reaches a maximum 40 mm below the bed top line. The devolatilisation zone extends 28 mm along the bed height. The maximum local devolatilisation rate in the constant stage is around 1.2×10^4 kg/m^{3}h; For the 35 mm fuel, the thickness of the devolatilisation zone increases to around 75 mm and the maximum local rate in the constant stage reduces to around 3.5×10^3 kg/m^{3}h, only a third of the level for the 10 mm fuel.

Fig. 6(e) and (f) illustrate the char burning rate distribution along the bed height as a function of time. The char combustion and gasification zone extends about 20 and 30 mm in the bed for the 10 and 35 mm fuels, respectively.

Fig. 7 shows the bed-height integrated process rates vs. reaction time for the two fuel sizes of 10 and 35 mm. The moisture evaporation rate rises to a peak value shortly after the over-bed ignition source is switched on and the other two sub-processes, i.e. volatile release and char burning follow consecutively. For the smaller fuel (Fig. 7(a), devolatilisation starts at $t=2.5$ min and the volatile release rate reaches an elevated and constant level at $t=6$ min. For the 35 mm fuel, devolatilisation starts at 3 min but the volatile release rate takes a much longer time (at $t=18$ min) to reach a stabilized level of around 165 kg/m^{2}h, which is compared to the average level of 185 kg/m^{2}h for the 10 mm fuel. As devolatilisation approaches completion, the two particle sizes demonstrate different behavior: the 10 mm particles illustrates a surge in volatile release while the 35 mm particles show a smooth decline in the devolatilisation rate. The smaller fuel also has an earlier start in char

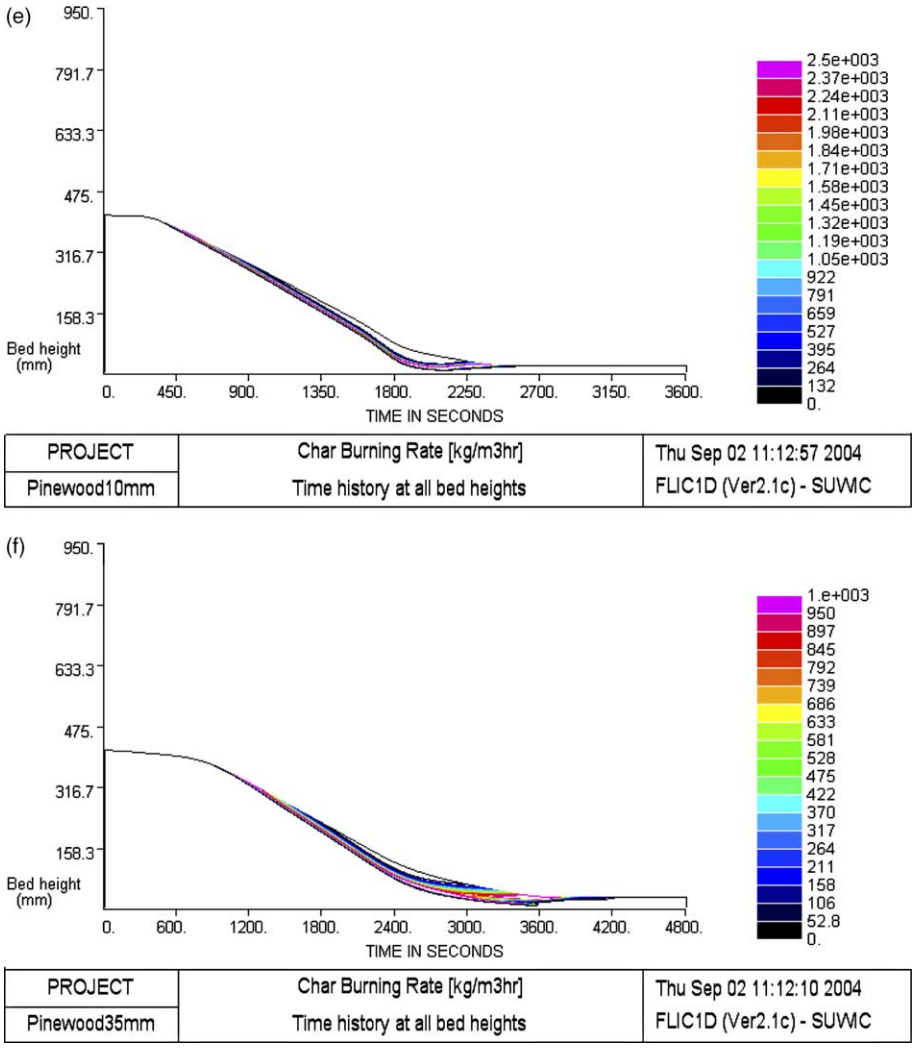

Fig. 6 (*continued*).

ignition and an overall higher char combustion/gasification rate than the bigger particles.

Fig. 7 also shows the calculated mass loss rate (including all the rates for the three sub-processes) compared to experimental measurements. The 10 mm particles feature a more constant and steady burning process during their major combustion stage while the 35 mm particles have most part of their combustion period undergoing gradual changes. Comparison between the modeling results and the measured ones are satisfactory for both the particle sizes.

6.2. Fuel size effect on major combustion parameters

Fig. 8 shows the fuel size effect on the average flame propagation speed during the major combustion stage (excluding the ignition and final burn-out periods). Experiments indicate a decreasing flame propagation speed with increasing particle size and the 35 mm fuel produced the lowest flame propagation speed of 150 kg/m^{2}h, compared to 205 kg/m^{2}h for the 5 mm fuel. The modeling prediction, however, shows the highest flame propagation speed is obtained at the fuel size of 10 mm. Consistency between experiments and predictions for the other three particle groups is fairly good, however.

Fig. 9 illustrates the fuel size effect on the average flame temperature during the major combustion stage (excluding the ignition and the final burn-out periods). Depending on the particle size, the measured level of flame temperature ranged from 810 to 900 °C and it is seen that fuel with a bigger size produced a higher combustion temperature. The model predicts the correct trend with variation in the particle size, but the calculated temperature level is 20∼30 °C higher than the measured ones, in general. This could be caused by the measurement error where the tips of the thermocouples were exposed to the cooler walls of the test rig and possibly gave a lower temperature reading.

Fig. 10 demonstrates the fuel size effect on the gas composition in the out-of-bed flue gases during the major combustion stage. A general trend is the declining CO concentration as particle size increased. The model

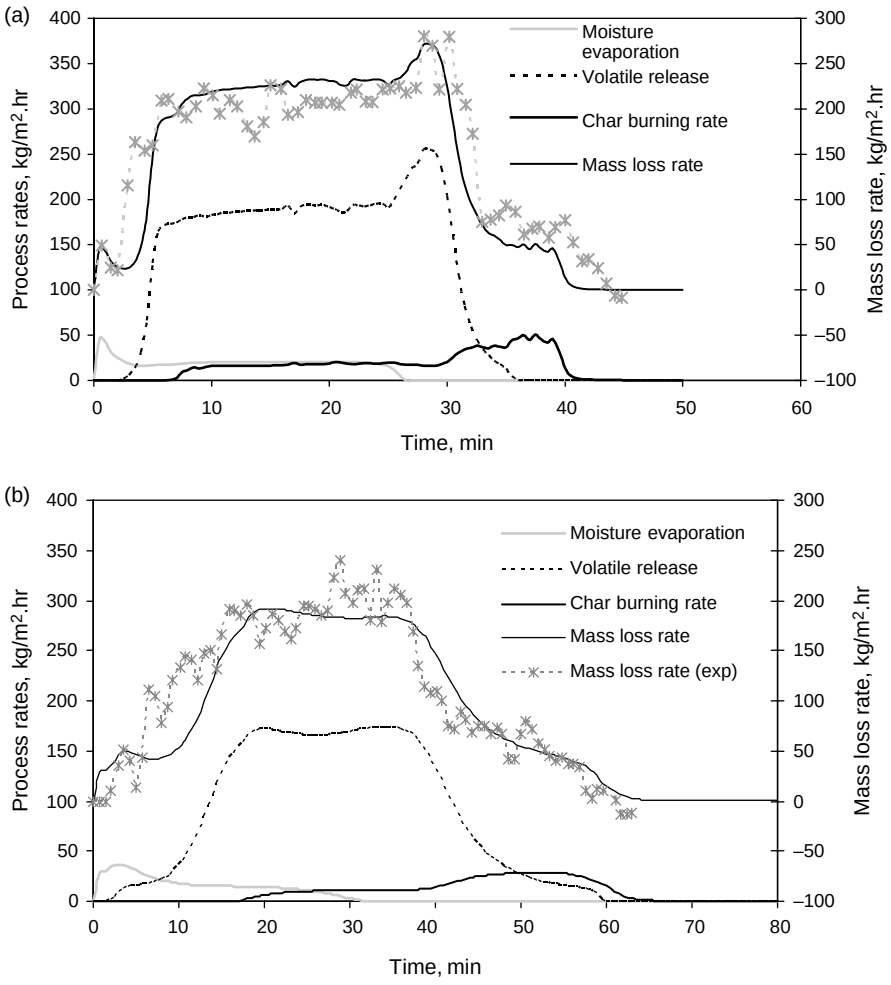

Fig. 7. Bed-height integrated process rates vs. reaction time. (a) 10 mm fuel; (b) 35 mm fuel.

predictions correctly reflect the measured trend but gives a slightly higher CO level across the whole size range.

Fig. 11 shows the predicted CH_4 and H_2 percentages in the out-of-bed flue gases as a function of fuel size. It is seen that the CH_4 concentration decreases with increasing fuel size, from 11% at 5 to 7.5% at 35 mm. The H_2 concentration, however, increases as fuel size increase, from 2.6% at 5 mm to 6.8% at 35 mm. Increasing in H_2 is due to slower mixing rate inside the bed of bigger size fuel between the H_2 and under-grate air. H_2 is both one of the primary devolatilisation products and the intermediate burning product of CH_4.

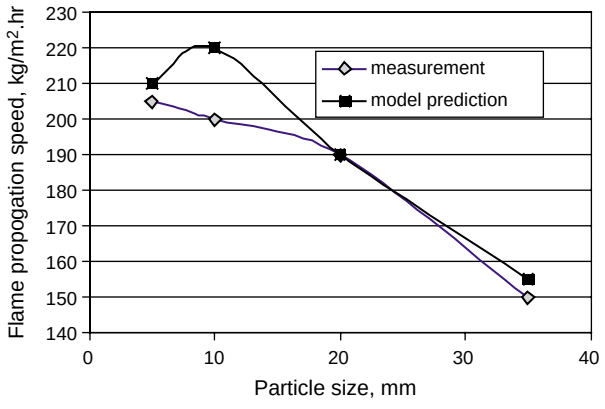

Fig. 8. Flame propagation speed vs. fuel size.

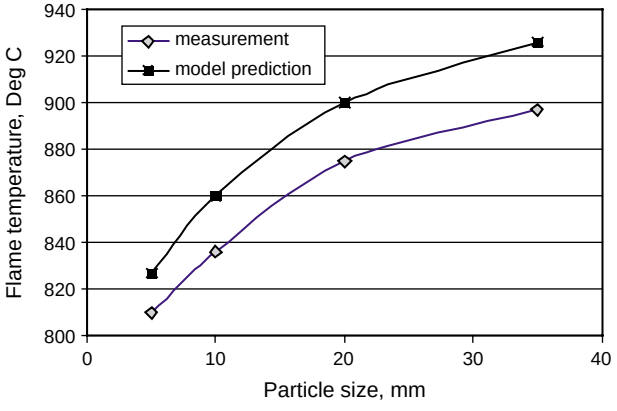

Fig. 9. Flame temperature vs. fuel size.

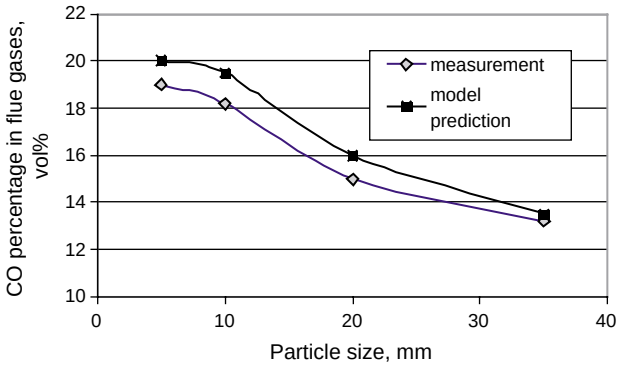

Fig. 10. CO percentage in the out-of-bed flue gases vs. fuel size.

7. Discussion and conclusions

The experiments demonstrated that a smaller size fuel tends to produce an earlier ignition of the bed than does a bigger size fuel, as indicated in Fig. 3. This is consistent with the experimental results of Friberg and Blasiak [4] where three different size fuels of wood were used. Mathematical modeling (Fig. 7) revealed that the smaller particle bed has a faster initial moisture evaporation rate when the over-bed ignition source is switched on so that the top surface of the bed is quicker to get dry and subsequently ignited. Similarly, dry-out of the whole bed is responsible for the temporally surge in the mass loss rate towards the end of the constant burning stage, as indicated by both the experiments and modeling prediction in Fig. 7 (more clearly for the case of 10 mm fuel).

Another obvious feature of the fuel size effect is that a bigger particle-size bed tends to burn transiently while a smaller particle-size bed can quickly build up a constant and steady burning pattern (Fig. 7). This finding is consistent with the results of Friberg and Blasiak [4]. This suggests that the control of a practical furnace firing bigger size fuels needs to be more carefully planned because of the constant variation of the burning pattern either with time if the bed is stationary or with bed length if the bed is moving. This can

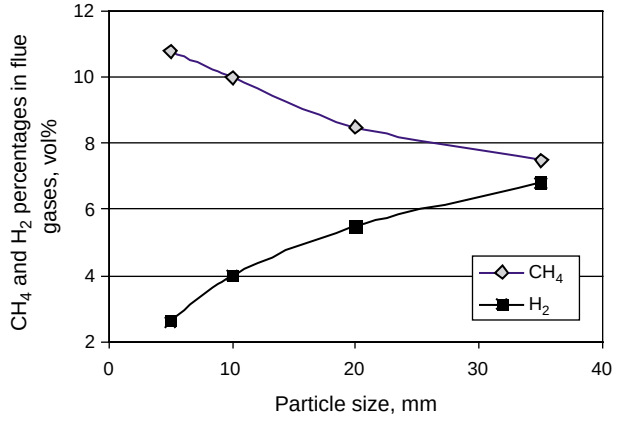

Fig. 11. Predicted CH_4 and H_2 concentrations in the out-of-bed flue gases vs. fuel size.

be explained by the ratio of the initial bed height to the reaction zone thickness. In the current experiments, this ratio is around 11.4 (410/36 mm) for the 10 mm fuel and 5.2 (410/78 mm) for the 35 mm fuel.

The measured flame propagation speed vs. particle size (Fig. 8) is consistent with the findings of Friberg et al. [4] who demonstrated decreasing burning rate as particles size increased. But the modelled trend is similar to the findings of Peters [12] who reported the maximum ignition rate obtained at 15 mm in the size range of 5–25 mm. However, the current results are contrary to the findings of Gort [3] and Rönnbäck et al. [5] who reported increased ignition speed for larger particles in the size range of 10–30 mm.

At the operating conditions of the current investigation, all fuels of the four sizes were burnt under sub-stoichiometric (fuel-rich) conditions. Understandably, a larger particle size produced a higher flame temperature (Fig. 9) as the burning rate slows down and the combustion shifts to less fuel-rich state.

Mathematical modeling results (Fig. 7) also reveal that a bed of small-particles has a distinctive final burning stage where all the moisture and volatile matter have been released but there is still a noticeable quantity of char remaining. The remaining char continues to burn until the total completion of the combustion process. For a bed of large-particles, however, the final burning stage features both the char burn-out and solid devolatilisation at the same time to a large extent. The knowledge of this difference is important because the operator of a real furnace has to plan the primary air distribution as correctly as possible for the emission control and optimization of the combustion efficiency.

In general, the following conclusions can be drawn from the current study in terms of the fuel size effect:

1. Ignition time is shorter with a bed of smaller particles than with larger particles at the same operating conditions;
2. Reaction zone is thicker with a larger-particle bed than with a smaller-particle bed;
3. Burning rate decreases with increase in fuel particle size;
4. Smaller fuel particles resulted in fuel-richer combustion and both higher CO and CH_4 concentrations in the out-of-bed flue gases; but the H_2 concentration decreases with decreasing in fuel size, according to model predictions;
5. Larger fuel particles produced higher burning temperature in the bed;
6. Small particles presented a uniform flame propagation speed during most part of the combustion process while large particles showed a more transient feature where the burning rate changes for most part of the combustion process;
7. In the final stage of the combustion, residual char burn-out is the only process occurring in a bed of small

particles. But in a bed of large particles, both char burnout and fuel devolatilisation occur at the same time.

Acknowledgements

This study was funded by EPSRC (UK) SuperGen Biomass Grant.

References

[1] Supergen web site: http://www.supergen-bioenergy.net/
[2] European Energy Crops InterNetwork: http://www.eeci.net/
[3] Gort R. On the propagation of a reaction front in a packed bed: thermal conversion of municipal waste and biomass. Academic Dissertation, University of Twente; 1995.
[4] Friberg R, Blasiak W. Measurements of mass flux and stoichiometry of conversion gas from three different wood fuels as function of volume flux of primary air in packed bed combustion. Biomass Bioenergy 2002;23:189–208.
[5] Rönnbäck M, Axell M, Gustavsson L. Combustion processes in a biomass fuel bed-experimental results. Progree in thermochemical conversion, Tyrol, Austria 2000 p. 17–22.
[6] Saastamoinen JJ, Taipale R, Horttanainen M, Sarkomaa P. Propagation of the ignition front in beds of wood particles. Combust Flame 2000;123:214–26.
[7] Van der lans RP, Pedersen LT, Jensen A, Glarborg P, Dam-Johansen K. Modelling and experiments of straw combustion in a grate system. Biomass Bioenergy 2000;19:199–208.
[8] Yang Y, Goodfellow J, Goh Y, Nasserzadeh V, Swithenbank J. Investigation of channel formation due to random packing in a burning waste bed. Trans IChemE, Part B 2001;79:267–77.
[9] Yang YB, Nasserzadeh V, Goodfellow J, Swithenbank J. Simulation of channel growth in a burning bed of solids. Trans IChemE, Part A 2003;81:221–32.
[10] Thunman H, editor. Principles and models of solid fuel combustion. Göteborg, Sweden: Chalmers University of Technology; 2001.
[11] Thunman H, Leckner B. Ignition and propagation of a reaction front in cross-current bed combustion of wet biofuels. Fuel 2001;80:473–81.
[12] Peters B. Thermal conversion of solid fuels.: WIT Press; 2003.
[13] Liang XH, Kozinski JA. Numerical modelling of combustion and pyrolysis of cellulosic biomass in thermogravimetric systems. Fuel 2000;79:1477–86.
[14] Yang YB, Nasserzadeh V, Goodfellow J, Goh YR, Swithenbank J. Parameter study on the incineration of municipal solid waste fuels in packed beds. J Inst Energy 2002;66–80.
[15] Yang YB, Yamauchi H, Nasserzadeh V, Swithenbank J. Effects of fuel devolatilisation on the combustion of wood chips and incineration of simulated municipal solid wastes in a packed bed. Fuel 2003;82:2205–21.
[16] Yang YB, Sharifi VN, Swithenbank J. Effect of air flow rate and fuel moisture on the burning behaviours of biomass and simulated municipal solid wastes in packed beds. Fuel 2004;83:1553–62.
[17] Behrendt Th. Thermodynamische modellierung des betriebsverhaltens einer hausmüllverbrennungsanlage am beispiel TAMARA. Fortschrittberichte reihe 15. Düsseldorf: VDI Verlag; 1992.
[18] Krüll F, Kremer H, Wirtz S. Feuerraumsimulation einer müllverbrennungsanlage bei gleichzeitiger simulation der verbrennung auf dem rost. VDI Bericht 1390, modellierung und simulation von dampferzeugern und feuerungen 1998 p. 199–212.
[19] Shin D, Choi S. The combustion of simulated waste particles in a bed. Combust Flame 2000;121:167–80.
[20] Goh YR, Siddall RG, Nasserzadeh V, Zakaria R, Swithenbank J, Lawrence D, et al. Mathematical modelling of the waste incinerator burning bed. J Inst Energy 1998.
[21] Adams T. A simple fuel bed model for predicting particulate emissions from a wood waste boiler. Combust Flame 1980;39:225–39.
[22] Stapf M, Kircherer A, Kolb Th, Wölfert A, Seifert H. Verbrennung im Drehrohrofen: modellierung, betriebs-und technikumsversuche. Volume 15 of VDI-Berichte 1313. Düsseldorf: VDI Verlag; 1997.
[23] Beckmann M, Scholz R. Simplified mathematical model of combustion in stoker systems. The third European conference on industrial furnaces and boilers. Porto, Portugal; 1995, p. 61–70.
[24] Wurzenberger JC. A combined packed bed and single particle model applied to biomass combustion. PhD thesis, Graz University of Technology; 2001.
[25] Peters B. A detailed model for devolatilization and combustion of waste material in packed beds. The third European conference on industrial furnaces and boilers (INFUB). Lisbon, Portugal; 18–21 April, 1995, p. 86–104.
[26] Hunt ML, Tien CL. Non-Darcian convection in cylindrical beds. J Heat Trans 1988;110:378–84.
[27] Vafai K, Sozen M. Analysis of energy and momentum transport for fluid flow through a porous bed. J Heat Trans 1990;112:690–9.
[28] Wakao N, Kaguei S. Heat and mass transfer in packed beds. London: Gordon & Breach; 1982.
[29] Blasi CD. Heat, momentum and mass transport through a shrinking biomass particle exposed to thermal radiation. Chem Eng Sci 1996;51:1121–32.
[30] Hottel HC, Sarofim AF. Radiative transfer. New York: McGraw-Hill Book Company; 1967.
[31] Yang YB, Goh YR, Zakaria R, Nasserzadeh V, Swithenbank J. Mathematical modelling of MSW incineration on a travelling bed. Waste Manage 2002;22:369–80.
[32] Smoot LD, Pratt DT. Pulverized-coal combustion and gasification. London: Plenum Press; 1979.
[33] Patankar SV. Numerical heat transfer and fluid flow. London, Washington: Hemisphere; 1980.
[34] Hornbeck RW. Numerical methods.: Quantum Publishers; 1975.
[35] Alves SS, Figueiredo JL. Pyrolysis kinetics of lignocellulosic materials by multistage isothermal thermo-gravimetry. J Analyt Appl Pyrol 1988;13:123–34.